

Coherent structures and turbulent molecular mixing in gaseous planar shear layers

By T. R. MEYER[†], J. C. DUTTON[‡] AND R. P. LUCHT[§]

Department of Mechanical and Industrial Engineering, University of Illinois
at Urbana-Champaign, Urbana, IL 61801, USA

(Received 29 October 2004 and in revised form 15 December 2005)

Quantitative planar visualization of molecular mixing dynamics in large- and intermediate-scale coherent structures is reported for the first time in the developing and far-field regions of gaseous planar shear layers. A dual-tracer (nitric oxide and acetone) planar laser-induced fluorescence (PLIF) technique is implemented as the gaseous analogue to acid/base chemical reactions that have previously been used to study molecular mixing in liquid shear layers. Data on low-speed, high-speed, and total molecularly mixed fluid fractions are collected for low- to high-speed velocity ratios from 0.25 to 0.44 and Reynolds numbers, Re_δ , from 18 600 to 103 000. Within this range of conditions, mixed-fluid probability density functions and ensemble-averaged statistics are highly influenced by the homogenizing effect of large-scale Kelvin–Helmholtz rollers and the competing action of intermediate-scale secondary instabilities. Small-scale turbulence leads to near-unity mixing efficiencies and mixed-fluid probabilities within the shear layer, with subresolution stirring being detected primarily along the interface with free-stream fluid. Current molecular-mixing data compare favourably with previous time-averaged probe-based measurements while providing new insight on the effects of coherent structures, velocity ratio, downstream distance, and differences between low- and high-speed fluid entrainment.

1. Introduction

Because of their simplicity, planar free shear layers are often used in numerical and experimental studies to represent the mixing process in fundamental flow fields found in many practical engineering applications. One of the most influential discoveries in this field involved the detection of a sudden increase in mixed-fluid quantities caused by the onset of small-scale turbulence within large-scale coherent motions (Konrad 1976). Subsequent experimental and numerical investigations have helped to decipher the complex nonlinear interactions that lead to this transition (Hussain & Zaman 1980; Huang & Ho 1990; Moser & Rogers 1991; Slessor, Bond & Dimotakis 1998; Dimotakis 2000; Meyer, Dutton & Lucht 2001). In the far-field self-similar region downstream of the mixing transition, the cascade to smaller turbulent length scales continues, and the concept of isotropic turbulence studied by Kolmogorov (1941) and Batchelor (1953) becomes relevant. This region is of fundamental interest to the turbulence modelling community and theoreticians because it sheds light

[†] Present address: Innovative Scientific Solutions, Inc., 2766 Indian Ripple Road, Dayton, OH 45440-3638, USA.

[‡] Present address: University of Texas at Arlington, Box 19018, Arlington, TX 76019-0018, USA.

[§] Present address: Purdue University, 585 Purdue Mall, West Lafayette, IN 47907-2088, USA.

on the elusive properties of fully developed turbulence. Studies at high Reynolds number ($Re_\delta > 30\,000$), for example, show evidence of mild to strong mixture-fraction inhomogeneities in the far-field region (Clemens & Mungal 1995; Karasso & Mungal 1996; King, Dutton & Lucht 1999). It is not clear how such mixing states are achieved, however, and the ambiguity is exacerbated by differences in experimental results.

The possible reasons for such disagreement are many, including Schmidt number differences between gases and liquids, planar versus axisymmetric shear-layer configurations, intrusive versus non-intrusive measurement techniques, time-averaged versus instantaneous experimental approaches, and differences in the spatial resolution of the measurements. Because of difficulties in resolving the smallest mixing scales, a number of investigations in gaseous and liquid flows have used chemical reactions to discern the true state of shear-layer molecular mixing. Numerous studies have used so-called acid/base visualizations to obtain comprehensive two-dimensional non-intrusive measurements of molecular mixing in turbulent liquid shear layers (Breidenthal 1981; Koochesfahani & Dimotakis 1986; Broadwell & Mungal 1988; Karasso & Mungal 1996). Owing to large differences in Schmidt number, Sc , results from these studies in liquids are not directly transferable to the case of gaseous shear-layer mixing. Previous studies in the latter regime are fewer in number and have relied on cold-wire measurements of low heat release reactions (Batt 1977; Mungal & Dimotakis 1984; Frieler 1992). The obvious disadvantages of this technique are the reliance on intrusive physical point probes and the inability to provide instantaneous planar images of molecular mixing. Previous investigations using the cold-wire approach have shown both marching (Batt 1977) and tilted (Frieler 1992) probability density functions (p.d.f.s) of mixed-fluid quantities, which indicate that different large and small-scale turbulent mixing dynamics may have been taking place in each of these experiments. An important motivation for the current investigation, therefore, is to provide planar images of molecular mixing and to enable deeper physical insight into the fundamental processes governing these statistics.

King, Lucht & Dutton (1997) developed a simultaneous dual-tracer nitric oxide (NO) and acetone planar laser-induced fluorescence (PLIF) technique that acts as the gaseous analogue of acid/base visualizations. With this technique, acetone PLIF is used as a passive-scalar marker of the mixture fraction within the shear layer, and NO PLIF is used as an optically reactive (i.e. cold-chemistry) marker of unmixed fluid. By subtracting the unmixed-fluid fraction from the passive-scalar (i.e. mixed plus unmixed) fluid fraction during post-processing, we can obtain instantaneous images of molecularly mixed fluid fraction across the entire width of the shear layer. King *et al.* (1999) successfully applied this technique to study near-field molecular mixing of turbulent jets with Reynolds numbers, Re_D , in the range of 1000 to 100 000. They noted two very distinct mixing regimes that were attributed to a mixing transition similar to that described by Konrad (1976). In a follow-up study, Meyer *et al.* (2001) investigated more closely the transitional regime between $Re_D = 16\,000$ and 30 000. They confirmed from mixed-jet-fluid statistics before, during, and after the cascade to small scales that, to first order, the location of this transition from the jet exit is inversely proportional to the initial instability wavelength of the jet shear layer.

The current investigation extends these studies of turbulent gaseous molecular mixing using the NO- and acetone-PLIF technique to planar shear layers. The planar case differs from axisymmetric jets in several respects: (i) planar shear layers have constant free-stream conditions and do not experience the effects of an increasing shear-layer thickness to diameter ratio; (ii) the enclosed planar shear-layer facility allows the seed species to be flipped for measurements of both low- and high-speed

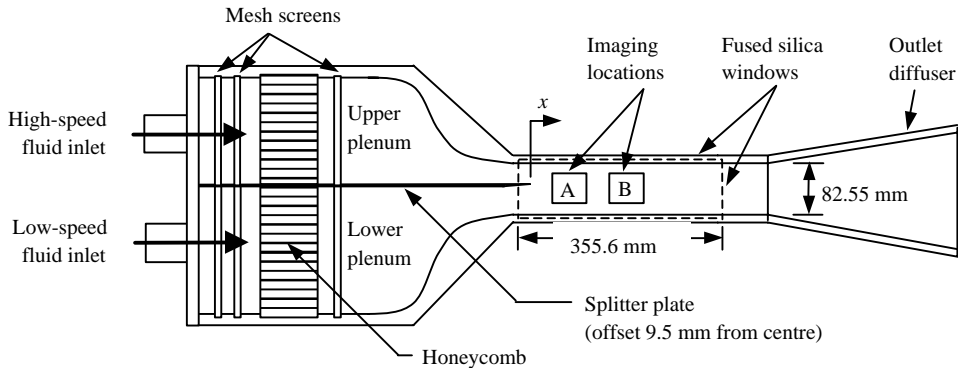


FIGURE 1. Schematic of the planar shear-layer facility. The cross-stream width is 101.6 mm.

fluid molecular mixing; (iii) the effect of velocity ratio can more readily be studied in the planar shear layer facility; and (iv) unlike jet measurements that are constrained to the region before the end of the jet potential core, measurements in planar shear layers can readily be performed in the far-field region.

The goal of this investigation is to provide a better understanding of the fundamental mechanisms that govern turbulent molecular mixing in incompressible gaseous planar shear layers, including the effects of coherent structures, Reynolds number, velocity ratio, initial instability wavelength and downstream distance. This is made possible by the use of simultaneous dual-tracer NO- and acetone-PLIF for the measurement of molecularly mixed fluid quantities along with instantaneous images across the entire width of the mixing layer. With this unique measurement capability, the interplay of large- and small-scale gaseous mixing phenomena can be studied directly, and the uncertainty due to subresolution stirring (pockets of pure fluid within the region imaged by a pixel element) is minimized. As with acid/base visualizations in liquid flows, this technique is also two-dimensional, non-invasive, time-resolved, and can be used to measure instantaneous mixed-fluid fractions in addition to time-averaged statistics.

After descriptions of the flow facility, measurement system, and flow conditions, we present and discuss the first two-dimensional measurements of low-speed, high-speed and total mixed-fluid statistics, time-averaged and instantaneous, in incompressible gaseous planar shear layers. Planar maps of molecular-mixing efficiency are used for the detection of small-scale subresolution stirring. The effect of coherent structures on the state of molecular mixing is further analysed through the use of probability density functions and time-averaged statistics. Comparisons are made with previous results from probe-based measurements of molecular mixing in gaseous planar shear layers, laser-based measurements of molecular mixing in gaseous axisymmetric shear layers, and laser-based measurements of molecular mixing in liquid planar shear layers.

2. Apparatus

2.1. Planar shear layer facility

The planar shear layer facility (figure 1) was initially built for compressible flow studies by Olsen (1999) and was subsequently modified for incompressible flow investigations by Meyer (2001). Compressed air from a PID-pressure-controlled

stagnation chamber passes through two mesh screens and a honeycomb block before entering the upper and lower plenum chambers via 76 mm diameter pipes. The plenum flow is further conditioned by passing through two mesh screens, a honeycomb block and a final mesh screen. The upper (high-speed) nozzle is 177.8 mm in height at the entrance and contracts to a height of 31.75 mm at the exit tip of the splitter plate, for a contraction ratio of 5.6:1. The lower (low-speed) nozzle is 227.1 mm in height at the entrance and contracts to a height of 50.8 mm at the exit tip of the splitter plate, for a contraction ratio of 4.5:1. The splitter plate is offset upward by 9.5 mm from the centre of the test section to compensate for the known deflection of the mixing layer toward the low-speed stream as a result of the continuity requirement. The spanwise dimension of the shear-layer test section is 101.6 mm, and the total height is 82.55 mm. All four walls of the test section have fused-silica windows for optical access in the ultraviolet. The total viewing length is 355.6 mm in the streamwise direction and begins slightly upstream of the splitter-plate tip. The flow exits the test section through a 610 mm long diffuser, enters the main exhaust line, and is vented to the exterior of the building.

The upper and lower plenum chambers are fed with either acetone-seeded air or NO-seeded nitrogen (N_2). The acetone seeding system consists of an atomizing nozzle located in the main air-supply pipe about 2 m upstream of the stagnation chamber to ensure complete vaporization and mixing. For the NO seeding system, nitrogen flow is supplied via an N_2 -cylinder manifold located about 5 m upstream of the 76 mm diameter supply pipe. Gas cylinders filled with 1000 p.p.m. NO-in- N_2 are diluted to 100–250 p.p.m. NO-in- N_2 , mixed in a swirl chamber, and conditioned with two mesh screens and a honeycomb block before entering the 76 mm supply pipe about 1 m upstream of the plenum chamber. The flow rate of the NO-in- N_2 gas was kept constant using a number of dual-stage regulators, as verified using hot-film measurements in the test section. Flip experiments are achieved by switching the seeded inlet flows to the 76 mm diameter pipes that feed the upper and lower plenum chambers.

2.2. NO/acetone PLIF measurement system

In a conventional passive-scalar (e.g. acetone) PLIF technique (Lozano, Yip & Hanson 1992), the detected LIF signal is linearly proportional to the tracer concentration, but the extent of molecular mixing is unknown since the smallest scales imaged are typically larger than the smallest diffusion scales. High-resolution measurements have been performed, but it is difficult to visualize molecular mixing at both the small and large scales simultaneously with this method (Dahm, Southerland & Buch 1991; Buch & Dahm 1996, 1998). In contrast to passive-scalar PLIF, cold-chemistry PLIF using NO seeding provides a measure of the extent of molecular unmixedness because its signal is highly quenched when it is molecularly mixed with oxygen (Paul & Clemens 1993). A 'flip' experiment can then be performed to obtain time-averaged total mixed-fluid-fraction statistics.

By using acetone PLIF as a passive-scalar measure of the fluid fraction from each fluid stream, and by using NO PLIF simultaneously as a measure of the unmixed fluid fraction from one fluid stream, instantaneous PLIF images of molecular mixing for the NO-seeded fluid can be obtained without resorting to a high-resolution imaging system (King *et al.* 1997). By performing the flip experiment, it is then possible to obtain instantaneous images of molecular mixing for both fluid streams. As this approach was initially being demonstrated, Island, Urban & Mungal (1996) proposed virtually the same idea but on a time-averaged basis. A similar approach that employs near-simultaneous passive-scalar acetone PLIF and cold-chemistry acetone

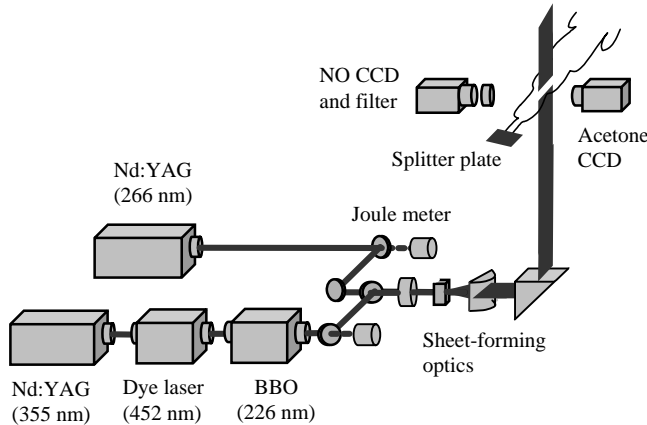


FIGURE 2. NO- and acetone-PLIF lasers and optics. BBO, beta barium borate crystal.

phosphorescence (Hu & Koochesfahani 2002) may also be considered as a gaseous analogue to acid/base reactions in that it can distinguish between fluid from each of the free streams. It is more easily implemented than the dual-tracer PLIF technique, but like other methods based on phosphorescence (Yip, Lozano & Hanson 1994), its limited temporal resolution can be a disadvantage for high-speed flows. The dual-tracer PLIF technique used here is to be distinguished from other multiple passive-scalar approaches (e.g. Seitzman *et al.* 1994) that fundamentally are neither intended for, nor are capable of, measuring the extent of molecular mixing. The theory and experimental set-up of the dual-tracer PLIF technique is fully described in the literature (King *et al.* 1997, 1999; Meyer *et al.* 1999, 2002); a brief summary is included below for reference.

As stated earlier, the shear flow consists of acetone-seeded air in one stream and NO-seeded N_2 in the other stream. Air is a convenient carrier for acetone because it quenches unwanted long-time-scale acetone phosphorescence and quenches NO PLIF upon molecular mixing within the shear layer. Nitrogen is a convenient carrier for NO because of its relatively small quenching cross-section. The technique requires coincident laser sheets at 226 nm and 266 nm for NO and acetone PLIF, respectively (figure 2). The NO PLIF signal from 226–300 nm is collected at 90° using a multi-element UV lens on an unintensified 512×512 CCD camera. The broadband acetone PLIF signal, centred at 450 nm, is collected simultaneously with the NO PLIF using a glass lens on a second CCD camera. For the current experiments, each camera images a $60 \text{ mm} \times 60 \text{ mm}$ physical region, which results in a probe area of $117 \mu\text{m} \times 117 \mu\text{m}$ per pixel. The probe depth is fixed by the NO and acetone laser-sheet thicknesses of $245 \pm 10 \mu\text{m}$, as measured by traversing a knife edge across the focal point. These values are well matched because differences in wavelength ($\sim 15\%$) and beam quality are offset by differences in beam diameter ($\sim 14\%$). Correspondingly, the focal depths differ by $\sim 3\%$.

Once acquired, the NO images are remapped to the same scale and orientation as the acetone images. This is accomplished to within pixel resolution using conformal mapping coefficients derived from a least squares fit to ~ 20 common points from images of aerosol scattering. After background subtraction to eliminate repeatable laser scatter, the NO and acetone PLIF signals from the mixing layer are normalized by reference signals from pure fluid regions. The latter normalization

is performed column-by-column and eliminates errors from shot-to-shot laser-sheet intensity variations as well as differences in camera sensitivity. As described above, the normalized and corrected acetone and NO PLIF signals represent the fraction of acetone-seeded fluid, f_{Ac} , and unmixed NO-seeded fluid, f_{uNO} , respectively. The mixed NO-seeded fluid fraction is then found from $f_{mNO} = f_{NO} - f_{uNO} = 1 - f_{Ac} - f_{uNO}$. By definition, the NO-seeded fluid molecular-mixing efficiency is the ratio of the molecularly mixed NO-seeded fluid to total NO-seeded fluid, or $\eta_{mNO} = f_{mNO}/f_{NO}$. Because NO is not fully quenched in the presence of small amounts of acetone and air, the final image-processing step is to perform a finite-quenching-rate correction for f_{uNO} based on an experimentally verified five-level model of NO fluorescence and the measured fluid fraction of acetone-seeded air (Meyer *et al.* 2002). At an acetone-seeded air fluid fraction of 5%, for example, the current dual-tracer PLIF approach predicts that about 10% of the NO signal remains unquenched. Accurate knowledge of the air fluid fraction and finite-quenching-rate effects, therefore, is one of the advantages of the current approach over previous measurements based on NO seeding alone (Clemens & Paul 1995; Island *et al.* 1996).

The signal-to-noise ratio (SNR) is typically 75:1 and 50:1 for the normalized acetone- and NO-PLIF images, respectively, in the corresponding free-stream regions. To estimate the uncertainty in f_{mNO} and η_{mNO} , one must account for both random errors associated with the SNR and bias errors due to image-matching (≤ 0.025), finite spatial resolution (≤ 0.01), sheet width (≤ 0.032), and differential diffusion of acetone and air in nitrogen (≤ 0.01). These errors are estimated based on the sensitivity in regions with high spatial gradients, and the error from differential diffusion is estimated from a direct numerical simulation of a jet mixing layer (Meyer *et al.* 2002). The final fractional uncertainties in f_{mNO} and η_{mNO} are highly dependent upon the local mixture fraction and can range from $\sim 6\%$ near the NO-seeded free stream to $\sim 19\%$ near the acetone-seeded freestream.

3. Flow conditions

Three velocity ratios (labelled 1, 2 and 3) and two downstream locations (labelled A and B) are studied in the current investigation, as shown in table 1. The high-speed fluid velocity is varied from about 30 to 50 ms^{-1} , while the low-speed fluid velocity is held nearly constant at about 13 to 14 ms^{-1} . Thus, flow conditions 1, 2 and 3 correspond to low- to high-speed velocity ratios, $r = U_{LS}/U_{HS}$, of 0.44, 0.34 and 0.25, respectively. Locations A and B at 80 mm and 178 mm downstream of the splitter-plate tip were selected to allow measurements early and late in shear-layer development while avoiding interaction with the channel walls. Dual-tracer PLIF images for flow conditions 1 and 3 were collected at both locations A and B, while data for flow condition 2 were collected at location B only. Based on these flow conditions and measurement locations, five pairing parameter values ranging from $Rx/\lambda = 6.6$ to 28.1 were investigated, as given in table 1. The pairing parameter is a non-dimensional downstream coordinate that accounts for the effects of velocity ratio and initial instability wavelength on the transition to small-scale turbulence (Karasso & Mungal 1996). The Reynolds number, which accounts for the effects of free-stream velocity difference and local shear-layer thickness, varies from $Re_\delta = 18\,600$ to 103 000, as given in table 1.

Characteristics of the boundary layers near the splitter-plate tip for both the low- and high-speed streams, as well as the downstream shear-layer velocity profiles, were measured using hot-film anemometry (Meyer 2001). The free-stream velocities

Parameter	Case		
	1 (Location A, B)	2 (Location B)	3 (Location A, B)
High-speed (HS) velocity, U_{HS} (m s^{-1})	29.5	42.0	50.5
Low-speed (LS) velocity, U_{LS} (m s^{-1})	12.8	14.1	12.8
Velocity ratio, $r = U_{LS}/U_{HS}$	0.44	0.34	0.25
Flip experiment performed	No, Yes	Yes	No, Yes
Velocity parameter, $R = (1 - r)/(1 + r)$	0.39	0.49	0.60
Initial instability wavelength, λ (mm)	4.7	4.1	3.8
Distance from splitter-plate tip, x (mm)	80, 178	178	80, 178
Pairing parameter, R_x/λ	6.6, 14.8	21.3	12.6, 28.1
2% – 98% mixing layer width, δ (mm)	16.7, 30.8	35.6	16.7, 41.4
Reynolds number, $Re_\delta = (U_{HS} - U_{LS})\delta/\nu$	18 600, 34 300	65 400	41 500, 103 000
Initial HS boundary-layer thickness, δ_{iHS} (mm)	1.4	1.2	1.1
Initial LS boundary-layer thickness, δ_{iLS} (mm)	2.6	2.6	2.6
Initial HS momentum thickness, θ_{iHS} (mm)	0.179	0.155	0.140
Initial LS momentum thickness, θ_{iLS} (mm)	0.32	0.32	0.32
Initial HS shape factor, $H_{iHS} = \delta_{iHS}^*/\theta_{iHS}\dagger$	2.33	2.49	2.56
Initial LS shape factor, $H_{iLS} = \delta_{iLS}^*/\theta_{iLS}\dagger$	2.58	2.58	2.58
Strouhal number, $St_\theta = \theta_{iHS}/\lambda$	0.038	0.038	0.038
Initial turbulence intensity, u'_i/U (%)	0.5–1.0	0.5–1.0	0.5–1.0
Pixel measurement area, L_{pix} (μm^2)	117×117	117×117	117×117
Laser sheet thickness, L_{las} (μm)	245 ± 10	245 ± 10	245 ± 10
Smallest diffusion length scale, L_D (μm)‡	140, 164	117	77, 96

† δ_i^* is the initial boundary-layer displacement thickness.

‡ $L_D = 11.2\delta Re_\delta^{-3/4} Sc^{-1/2}$ (from Buch & Dahm 1998).

TABLE 1. Flow conditions.

remained uniform across the test section to within about 1%. The shape factor of the low-speed boundary layer, $H = 2.58$, matches that of a laminar (i.e. Blasius) profile. The shape factor for the high-speed boundary layer deviates by as much as 10% from a Blasius profile for flow condition 1, but is quite close to the Blasius profile for flow conditions 2 and 3. Table 1 gives these and other relevant boundary-layer and shear-layer parameters for comparison with other experimental investigations.

The initial instability wavelength, λ , varies with the high-speed fluid velocity, and is estimated from acetone PLIF visualizations of the initial vortex spacing, λ_{vis} , near the splitter-plate tip. Although it is difficult to obtain a ‘true’ measurement of λ for comparison with flow conditions from other facilities, a good estimate of λ was obtained by measuring the high-speed boundary layer momentum thickness, θ_{iHS} , near the splitter-plate tip. The results for flow conditions 1 to 3 are plotted in figure 3 and reliably fit the relation $\lambda_{vis} \approx 26\theta_{iHS}$. Many of the results in this work are compared with the acid/base liquid mixing-layer visualizations and measurements of Karasso & Mungal (1996), who used $\lambda_{vis} \approx 30\theta_{iHS}$. Mehta *et al.* (1987) used $\lambda_{vis} \approx 25\theta_{iHS}$ in a gaseous mixing layer, while a variety of other investigators have used other values near or within this range (Gutmark & Ho 1983). The expected linear dependence of λ on $U_{HS}^{-1/2}$ for laminar boundary layers is also shown in figure 3. Thus, the values of λ shown in table 1 should not only provide an appropriate instability length scale for the current investigation, but should also provide an approximate scaling for comparison with results from other facilities.

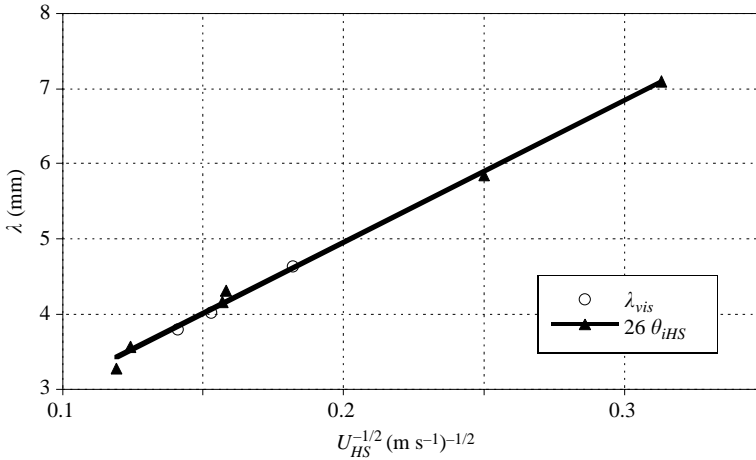


FIGURE 3. Variation of the initial instability wavelength, λ , with $U_{HS}^{-1/2}$. Initial vortex spacing, λ_{vis} , is compared with the relation $\lambda = 26\theta_{iHS}$.

The range of flow conditions given in table 1 was selected to allow measurements in the developing and fully developed turbulent regimes, the latter of which has been shown in past studies in gaseous and liquid mixing layers to require a minimum $Re_\delta \approx 10000$ (Slessor *et al.* 1998). All the flow conditions examined in this study are above this value. Other investigators have found, however, that hydrodynamic quantities become fully-developed at $Rx/\lambda \approx 8$ to 16 (Huang & Ho 1990; Karasso & Mungal 1996), while scalar quantities become fully developed by $Rx/\lambda \approx 22$ (Karasso & Mungal 1996). Thus, for Case 1A ($Rx/\lambda \approx 6.6$), fully developed hydrodynamic conditions may not be attained even though $Re_\delta > 10000$. Furthermore, Case 2B ($Rx/\lambda \approx 21.3$) is at the threshold for being fully developed in terms of scalar quantities, while only Case 3B ($Rx/\lambda \approx 28.1$) is beyond both the Re_δ and Rx/λ criteria for fully developed hydrodynamic and scalar quantities.

Another condition for self-similarity, proposed by Bradshaw (1966), states that the downstream distance from the splitter-plate tip must be greater than $1000\theta_{iHS}$. Subsequent studies have proposed criteria for self-similarity as high as $2000\theta_{iHS}$ or more (Dziomba & Fiedler 1985), although Bradshaw's original hypothesis has been found to hold true for laminar (Blasius-type) initial conditions. Thus, for the laminar conditions documented in the current study, Case 2B ($x \approx 1000\theta_{iHS}$) is again at the threshold for being fully developed, based on this criterion, while Case 3B ($x \approx 1300\theta_{iHS}$) is beyond this threshold. In fact, Bradshaw's criterion and that of the pairing parameter are identical insofar as the initial instability wavelength is directly proportional to θ_{iHS} , as shown in figure 3.

Another factor that has been shown to affect the development of mixing layers is the finite thickness of the splitter-plate tip. This thickness is more important for higher velocity ratios ($r > 0.6$), for which the splitter-plate wake has been found to have a lasting effect on the three-dimensional structure of the mixing layer (Wiecek & Mehta 1998). At $r = 0.44$, which is equivalent to the highest velocity ratio for the current study, Dziomba & Fiedler (1985) found that the trailing-edge thickness can affect shear-layer development if it exceeds 50% of the total (low- and high-speed) boundary-layer displacement thickness. The splitter-plate thickness (0.35 mm) is less than 30% of the total boundary-layer displacement thickness for all of the flow conditions in the current study and thus should not play a significant role in the far-field mixing dynamics.

Of final concern for the initial conditions is the initial free-stream turbulence intensity level, u'_i/U , which is shown in table 1 to vary between 0.5 and 1%. Mehta (1991) has suggested that $u'_i/U < 0.2\%$ is required for the mixing-layer development to be independent of the velocity ratio. At the lower velocity ratios in the current study ($r < 0.5$), the local turbulence intensity in the mixing layer is much greater than the free-stream turbulence level and is more likely to develop independently of u'_i/U . Nonetheless, it is difficult to determine an exact threshold velocity ratio for which the effects of free-stream turbulence become significant, and this factor must be kept in mind when comparing the data at various velocity ratios from this and other investigations.

4. Instantaneous images

Representative instantaneous images from the dual-tracer PLIF technique for all of the conditions given in table 1 are shown in figures 4–7, with sample line plots in figure 8. The fractions of low- and high-speed fluid are represented by f_{LS} and f_{HS} , respectively, and sum to unity for the current binary fluid system. When acetone is seeded into the high-speed stream, f_{HS} is found directly from the normalized and corrected acetone-PLIF image and $f_{LS} = 1 - f_{HS}$. In this case, NO is seeded into the low-speed stream so that the fraction of unmixed low-speed fluid, f_{uLS} , is found from the normalized and corrected NO-PLIF image. From these two images, it is then possible to compute the fraction of molecularly mixed low-speed fluid from $f_{mLS} = f_{LS} - f_{uLS}$, as well as the low-speed fluid molecular-mixing efficiency, $\eta_{mLS} = f_{mLS}/f_{LS}$, which is also plotted in figures 4 to 8. By definition, η_{mLS} is unity when all of the NO-seeded fluid in a measurement volume is mixed at the molecular level (i.e. $f_{mLS} = f_{LS}$); non-unity values of η_{mLS} imply the existence of pure-fluid subresolution stirring. The flip experiment is accomplished simply by seeding acetone and NO in the opposite streams so that the PLIF images can be used to obtain f_{mHS} and η_{mHS} .

4.1. Primary and secondary entrainment

One of the more striking features in the passive-scalar images of Pickett & Ghandhi (2002) in moderate-speed gaseous planar shear layers is the existence of both primary and secondary structures associated with the original Kelvin–Helmholtz instability and localized shear layers, respectively. A similar observation can be made regarding the higher Re_δ conditions of the current study, as shown in figures 4 to 7. Superimposed on the large-scale roll-up of figure 5(a) are intermediate-scale structures with sizes of $\sim 0.1\delta$, some of which are identifiable as vortex roll-ups, but most of which are of random shape and orientation. These intermediate-scale structures, which may have their origin in the collapse of streamwise vortices (Moser & Rogers 1991), enhance mixing along the outer region of the shear layer such that large-scale roll-ups entrain mixed rather than unmixed fluid. This is illustrated further in figures 6(b) and 7(b), which show low-speed fluid being entrained intermittently. The result is a convoluted internal mixing layer with fluid structures that originate from the edge of the shear layer and that continue the transition to small-scale mixing through further interaction. The line plots of figure 8 are representative of this convoluted internal structure, with low-speed fluid being preferentially entrained on the low-speed side and high-speed fluid being preferentially entrained on the high-speed side. At various instances, the shear layer intermittently displays a predominant large-scale structure, as in figure 6(b), or a lack of large-scale organization, as in figure 6(a). In the absence of a large-scale Kelvin–Helmholtz roll-up, intermediate-scale structures enhance the

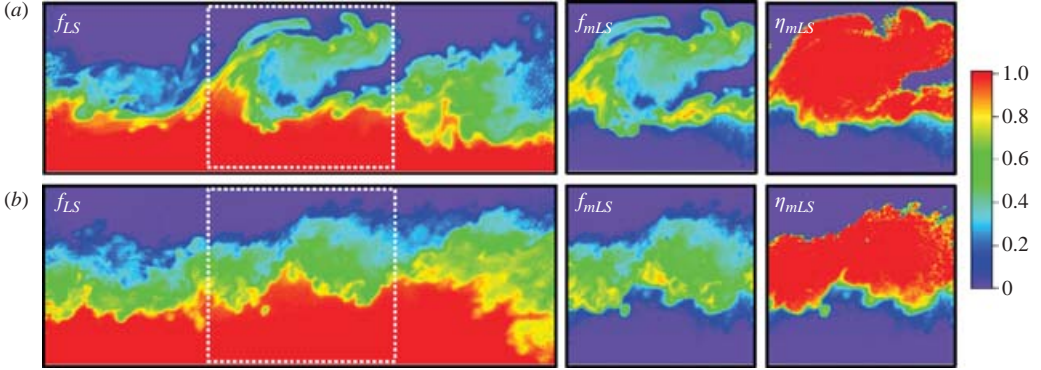


FIGURE 4. Instantaneous images of total low-speed fluid fraction, f_{LS} , mixed low-speed fluid fraction, f_{mLS} , and low-speed fluid molecular-mixing efficiency, η_{mLS} , for (a) Case 1A ($Re_\delta = 18\,600$, $Rx/\lambda = 6.6$) and (b) Case 3A ($Re_\delta = 41\,500$, $Rx/\lambda = 12.6$). Streamwise extent is $x = 50\text{--}110$ mm and cross-stream extent is $y/\delta = \pm 0.5$.

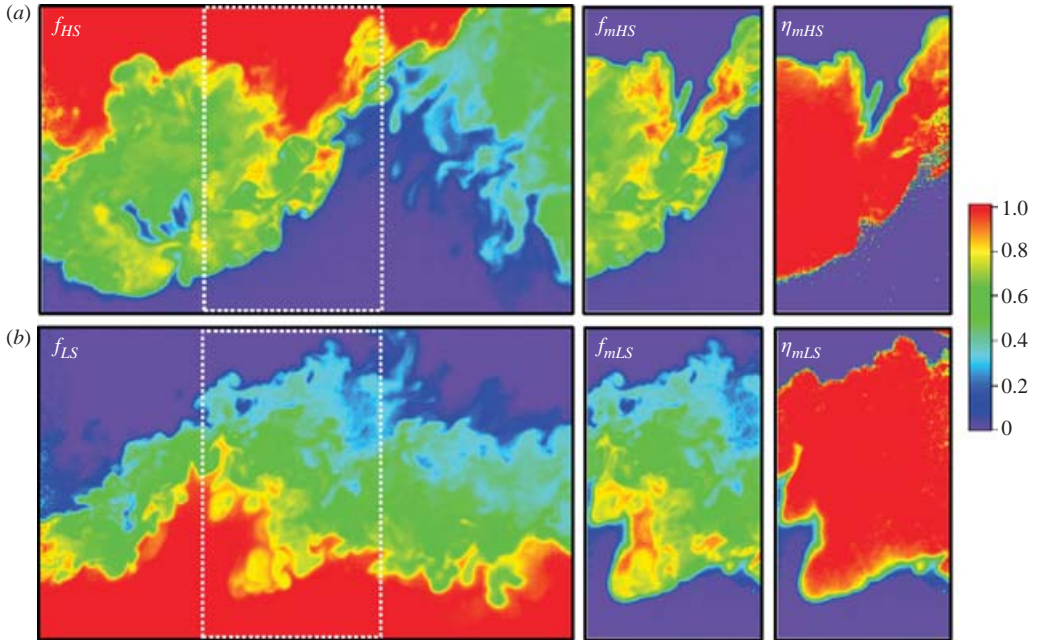


FIGURE 5. Instantaneous time-uncorrelated images of the flip experiment for Case 1B ($Re_\delta = 34\,300$, $Rx/\lambda = 14.8$) with NO seeded into (a) the high-speed stream and (b) the low-speed stream. Streamwise extent is $x = 148\text{--}208$ mm, and cross-stream extent is $y/\delta = \pm 0.5$.

entrainment of free-stream fluid into the outer regions of the shear layer and imply the existence of non-stationary mixed-fluid p.d.f.s.

These observations differ from the classical descriptions of Broadwell & Breidenthal (1982) and Masutani & Bowman (1986), whose data suggest that fluid in the mixing layer is composed of either pure fluid, homogeneously mixed fluid, or interfacial

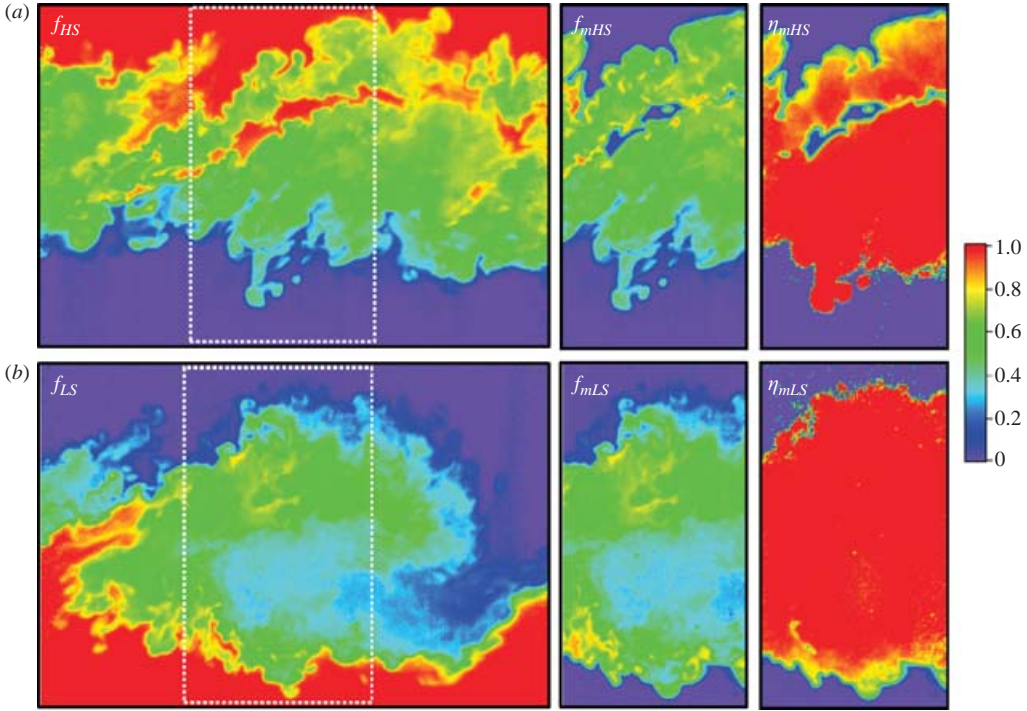


FIGURE 6. Instantaneous time-uncorrelated images of the flip experiment for Case 2B ($Re_\delta = 65\,400$, $Rx/\lambda = 21.3$) with NO seeded into (a) the high-speed stream and (b) the low-speed stream. Streamwise extent is $x = 148\text{--}208$ mm and cross-stream extent is $y/\delta = \pm 0.5$.

diffusion layers between the pure and mixed fluids. The images shown in figures 4 to 7 indicate that the interfacial diffusion layers may be dominated by intermediate-scale secondary instabilities. The existence of intermediate-scale vortices leads to regions of inhomogeneously mixed fluid of widely varying concentration, as is shown in figure 8. A similar observation regarding the effects of primary and secondary structures was made by Meyer *et al.* (2001), who reported the frequent occurrence of two predominant mixed-fluid concentrations across axisymmetric gaseous mixing layers. In the current planar shear-layer data, instantaneous images show a wider variation in mixed-fluid concentrations associated with secondary instabilities as compared with the axisymmetric shear-layer results of Meyer *et al.* (2001). The size and frequency of primary and secondary structures have implications for the statistical character of the planar mixing layer, as discussed further in terms of probability density functions and ensemble-averaged statistics in § 5 and § 6, respectively.

4.2. Mixing efficiency and subresolution stirring

The dynamics of primary and secondary instabilities have important implications for the existence of subresolution stirring as large- and intermediate-scale structures entrain pure fluid at varying depths within the shear layer. Figure 4 shows typical instantaneous images of the low-speed fluid fraction, f_{LS} , mixed low-speed fluid fraction, f_{mLS} , and low-speed fluid molecular-mixing efficiency, η_{mLS} , for location A ($x = 80$ mm). The fluid fractions and molecular-mixing efficiency for the high-speed

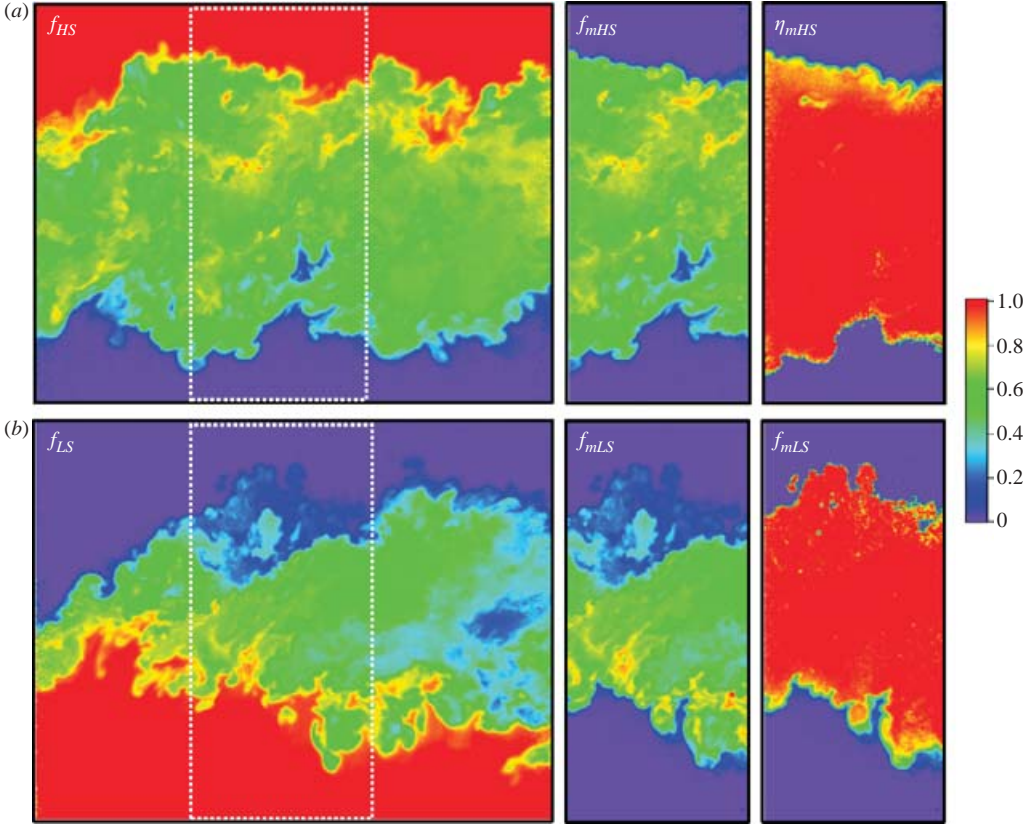


FIGURE 7. Instantaneous time-uncorrelated images of the flip experiment for Case 3B ($Re_\delta = 103\,000$, $Rx/\lambda = 28.1$) with NO seeded into (a) the high-speed stream and (b) the low-speed stream. Streamwise extent is $x = 148\text{--}208$ mm and cross-stream extent is $y/\delta = \pm 0.5$.

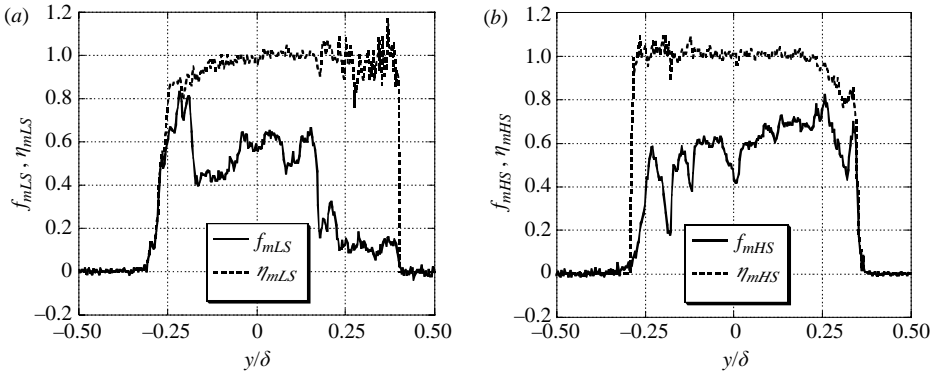


FIGURE 8. Sample cross-stream profiles of (a) f_{mLS} and η_{mLS} and (b) f_{mHS} and η_{mHS} for Case 3B ($Re_\delta = 103\,000$, $Rx/\lambda = 28.1$) collected at the central x location of figure 7. Negative y/δ toward the low-speed stream.

fluid are not presented because flip experiments were not performed for these conditions (see table 1). Note the increase in small-scale turbulence from Case 1A in figure 4(a) to Case 3A in figure 4(b). This increase corresponds to a change in pairing parameter from $Rx/\lambda = 6.6$ to 12.6 and a change in Reynolds number

from $Re_\delta = 18\,600$ to $41\,500$. Indeed, the smallest diffusion length scale is expected to decrease from $140\ \mu\text{m}$ to $77\ \mu\text{m}$ under these conditions, as shown in table 1. The limiting resolution of $245\ \mu\text{m}$, as defined by the laser sheet thickness, cannot fully resolve these scales. Nonetheless, images of f_{LS} (obtained from acetone PLIF) and f_{mLS} (obtained from NO and acetone PLIF) are nearly identical within the mixing layer. As a result, maps of low-speed-fluid molecular-mixing efficiency, $\eta_{mLS} = f_{mLS}/f_{LS}$, are nearly unity throughout most of the internal regions of the shear layer for Cases 1A and 3A. It is possible to conclude, therefore, that subresolution stirring of molecularly unmixed low-speed fluid is found primarily along the outer edges along the interface between the mixing layer and the low-speed (NO-seeded) fluid stream. This interface is also the region with the least uncertainty in both f_{mLS} and η_{mLS} ($\sim 6\%$). Subresolution stirring of low-speed fluid is not detected near the high-speed (acetone-seeded) fluid stream, presumably because all of the low-speed fluid in this region is molecularly mixed.

Instantaneous images with the same seeding configuration as for figure 4, as well as with the acetone- and NO-seeded flows flipped, are available at location B, which is $100\ \text{mm}$ downstream of location A. This ‘flip’ experiment provides images of molecularly mixed high- and low-speed fluid, as well as time-averaged statistics of the total amount of molecularly mixed fluid. These images and associated statistics are the first to be obtained in a planar or axisymmetric gaseous shear layer and are used to resolve previous ambiguities regarding the relative molecular mixing behaviour of the high- and low-speed fluids. Figure 5 shows sample instantaneous time-uncorrelated flip images for Case 1B ($Re_\delta = 34\,300$, $Rx/\lambda = 14.8$). As shown in table 1, the shear-layer width has grown by nearly a factor of two from Case 1A in figure 4(a) to Case 1B in figure 5(b). Correspondingly, the fluid structures within the mixing layer and at the mixing-layer-to-free stream interfaces have also increased in size. This leads to an increase in diffusion length scale from Case 1A to 1B as given in table 1. Although the images are still underresolved, near-unity maps of low- and high-speed fluid molecular-mixing efficiency again indicate that subresolution stirring of pure fluid is confined to the outer regions of the mixing layer adjacent to the NO-seeded free stream.

The shear-layer width grows for Cases 2B ($Re_\delta = 65\,400$, $Rx/\lambda = 21.3$) and 3B ($Re_\delta = 103\,000$, $Rx/\lambda = 28.1$), as shown in figures 6 and 7, respectively. According to table 1, the smallest diffusion length scale should decrease by $\sim 30\%$ from Case 1B to 2B and by $\sim 40\%$ from Case 1B to 3B because of increasing Re_δ . Despite the presence of smaller diffusion length scales, no increase in subresolution stirring of pure low- or high-speed fluid is detected in the internal regions of the mixing layer. This is verified in the line plots of figure 8, in which only the outer low- and high-speed regions have sub-unity values of η_{mLS} and η_{mHS} , respectively. As will be discussed further in §6, this implies that the total mixed-fluid probability should be near unity for the internal regions of turbulent gaseous planar shear layers.

In previous studies of gaseous axisymmetric shear layers, King *et al.* (1999) and Meyer *et al.* (2001) also found near-unity mixing efficiency of high-speed fluid using the dual-tracer PLIF technique. Data collected with NO seeded into the high-speed jet showed unity values of η_{mHS} throughout most of the mixing layer, including the vortex roll-up, pairing, breakup, transitional and turbulent regions. As is the case in the current study, sub-unity values of η_{mHS} were detected primarily in a thin region along the interface between the mixing layer and the high-speed (NO-seeded) fluid stream. As stated in §1, the flip experiment was not performed by King *et al.* (1999) or Meyer *et al.* (2001), and so it is not possible to compare the low-speed fluid

molecular-mixing efficiency results for the planar and axisymmetric cases. Based on the data presented in figures 5 to 7, however, it is likely that near-unity low-speed mixing efficiencies are also typical throughout the internal regions of fully developed turbulent gaseous axisymmetric shear layers.

5. Probability density functions

Probability density functions of various fluid quantities are useful for detecting statistically relevant trends in the mixing process. Such trends can then be related to the instantaneous images of molecularly mixed fluid fraction and molecular-mixing efficiency discussed in §4. The probability density function of molecularly mixed NO-seeded fluid, f_{mNO} , is normalized to unity,

$$\int_0^1 P(f_{mNO}, x, y) df_{mNO} = 1, \quad (1)$$

where x and y for a digital image denote a pixel location in the mixing layer. When NO is seeded into the low- or high-speed stream, f_{mNO} is represented by f_{mLS} or f_{mHS} , respectively. Unlike ensemble-averaged quantities, which can mask large-scale structure intermittency, p.d.f. shapes show the likelihood of finding pure fluid (tagged as 0 or 1), indicate the range of f_{mNO} values found at a particular location (by a narrow or broad shape), and show the most likely or preferred f_{mNO} value at a particular location (from the peak in the profile). By analysing the changes in p.d.f. shape across a mixing layer, therefore, one can detect changes in the character of the intermittent mixing process and compare observations with other investigations. Differences in the processes of entrainment and mixing between the low- and high-speed fluids can also be obtained for the current experiments by flipping the NO-seeded fluid between the low- and high-speed streams.

Probability density functions for each condition given in table 1 were calculated from ensembles of about 100 images, concentration bin widths of 2.5 %, and spatial bin sizes of 350 μm (3 pixels) in the x and y directions. The concentration and spatial bin sizes are of the same order as the limiting SNR and imaging resolution, respectively, and allow for reasonably smooth p.d.f.s. All p.d.f.s presented herein were obtained at the centre- x location of the images. Each plot contains multiple p.d.f.s ranging from $y/\delta = \pm 0.5$ in the cross-stream direction (with negative values of y/δ toward the low-speed stream).

5.1. Effect of velocity ratio and downstream distance

Figure 9(a) shows p.d.f.s of the low-speed mixed-fluid fraction, $P(f_{mLS})$, for Case 1A ($r = 0.44$); the lower velocity-ratio condition of Case 3A ($r = 0.25$) is shown for comparison in figure 9(b). The decrease in velocity ratio means that the shear layer is more fully developed for Case 3A, with Re_δ increasing from 18 600 to 41 500 and the pairing parameter increasing from 6.6 to 12.6. The following is a detailed description of how p.d.f. trends in the cross-stream direction relate to shear-layer mixing dynamics and how these trends change with velocity ratio from Case 1A to 3A. On the high-speed side of figure 9(a) from $y/\delta = 0.1$ to 0.5, peaks in $P(f_{mLS})$ are found at f_{mLS} values of either 0 % or 35 %. These values represent times when the measurement volume is either within pure high-speed fluid entrainment regions, indicating the presence of large Kelvin–Helmholtz vortices, or within mixed-fluid structures, respectively. The peak near 35 % remains stationary as y/δ decreases, but at the centre of the mixing layer (near $y/\delta = 0$) the p.d.f. shape broadens and the

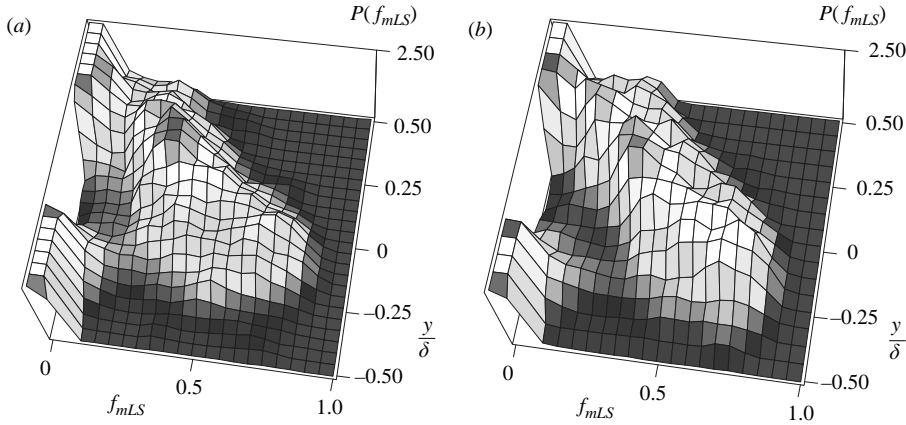


FIGURE 9. Cross-stream p.d.f.s of f_{mLS} for (a) Case 1A ($Re_\delta = 18\,600$, $Rx/\lambda = 6.6$) and (b) Case 3A ($Re_\delta = 41\,500$, $Rx/\lambda = 12.6$).

peak f_{mLS} shifts to about 40%. The slight shift from 35% to 40% represents tilted p.d.f. behaviour, signifying a non-uniform mixed-fluid composition across the shear layer. Few, if any, f_{mLS} values of 0% occur in this central region, which is indicative of reduced pure-fluid intermittency. On the low-speed side (toward $y/\delta = -0.5$), the peak at 40% diminishes and a second peak appears at an f_{mLS} of 70%, signifying increased entrainment of low-speed fluid within the shear layer. As discussed in §4.2, such preferential entrainment of low-speed fluid toward the low-speed free stream is indicative of intermediate- or small-scale mixing along the outer region of the mixing layer. The existence of intermediate scale-mixing in this region is apparent in the planar maps of figures 4 to 7, while the existence of small-scale mixing is confirmed by the presence of sub-unity molecular mixing efficiencies reported earlier in §4.2. The dual peaks at f_{mLS} of 40% and 70% toward the low-speed edge of the mixing layer represent the respective competition between large-scale Kelvin–Helmholtz vortices and intermediate- or small-scale structures induced by local turbulence.

For the lower velocity ratio of Case 3A in figure 9(b), the p.d.f.s of f_{mLS} take on a marching character from a peak at nearly 0% on the high-speed side to 70% on the low-speed side. This marching character results from a breakdown of large-scale Kelvin–Helmholtz vortices and the increased dominance of secondary entrainment, as shown in figure 4(b) and discussed in §4.2. Similar observations about the breakdown of large roller structures and the emergence of marching p.d.f.s are reported in the direct numerical simulation data of Rogers & Moser (1994).

The effect of velocity ratio can also be shown further downstream at location B, where flip experiments were performed for Cases 1B ($r = 0.44$) and 3B ($r = 0.25$); mixed-fluid p.d.f.s for these conditions are shown in figures 10(a) and 10(b), respectively. The effect of velocity ratio on the low-speed fluid p.d.f.s is very similar to that observed for Cases 1A and 3A, as described above in detail. The high-speed fluid p.d.f.s evolve from a stationary to a hybrid character in which the peak $P(f_{mHS})$ begins to march to lower values of f_{mHS} toward the low-speed stream. This marching behaviour signifies a slight decrease in the influence of large-scale structures and an increase in the influence of secondary entrainment for more fully developed turbulent conditions. The p.d.f.s for Case 3B are also narrower than for Case 1B, signifying reduced intermittency associated with a breakdown of large-scale vortices.

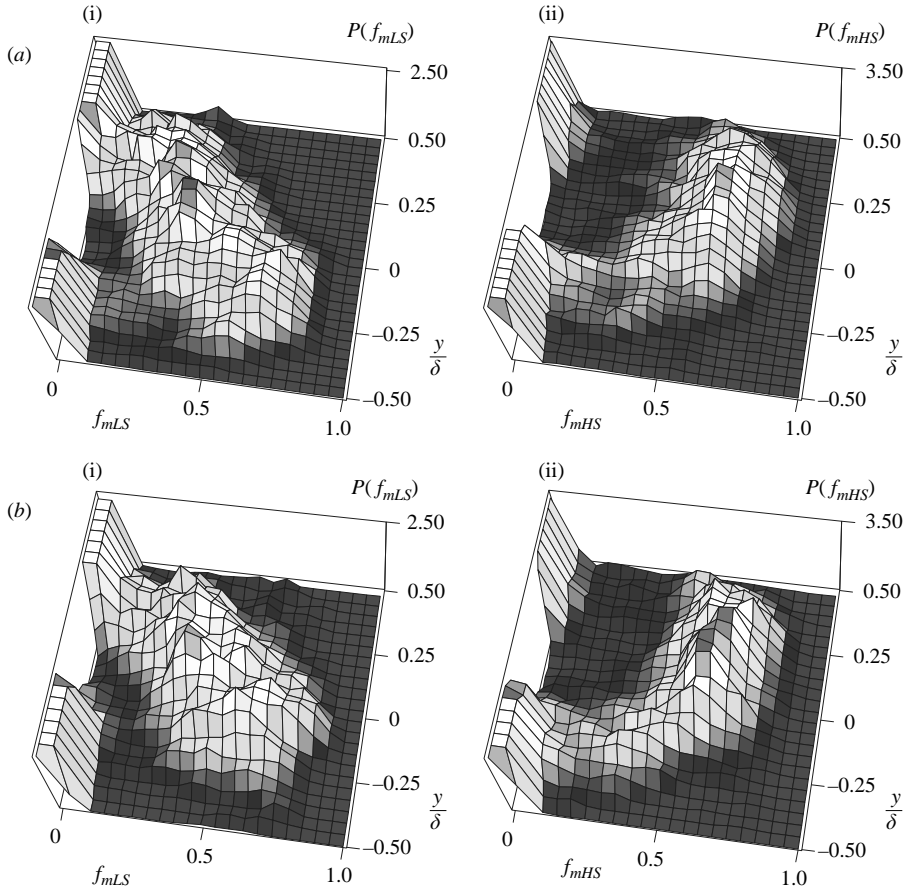


FIGURE 10. Cross-stream p.d.f.s of f_{mLS} and f_{mHS} for (a) Case 1B ($Re_\delta = 34\,300$, $Rx/\lambda = 14.8$) and (b) Case 3B ($Re_\delta = 103\,000$, $Rx/\lambda = 28.1$). (i) low-speed fluid; (ii) high-speed fluid.

The effect of downstream distance is not dramatic for Cases 1A and 1B, which have the same inflow conditions, but are separated by 100 mm in the streamwise direction. The low-speed fluid p.d.f.s of Case 1A in figure 9(a) are surprisingly similar to the p.d.f.s of Case 1B in figure 10(a). Indeed, the fluid structures in figures 4(a) and 5(b) show that the primary and secondary entrainment processes are quite similar despite a significant change in the shear-layer width with downstream distance. These observations are consistent with the concept of self-similarity for fully developed turbulence.

Comparison with the dual-tracer PLIF results of King *et al.* (1999) and Meyer *et al.* (2001) indicate that the effect of downstream distance is somewhat different in the case of gaseous axisymmetric shear layers. The character of the high-speed mixed-fluid p.d.f.s shown in figure 10 for the current investigation is predominantly stationary, with a slight increase in marching behaviour on the low-speed side at the more fully developed condition of figure 10(b). King *et al.* (1999) and Meyer *et al.* (2001) recorded similar molecularly mixed high-speed-fluid p.d.f. shapes in axisymmetric gaseous jets, but with stronger marching behaviour on the low-speed side. Instantaneous plots of molecularly mixed high-speed fluid fraction from these studies displayed homogeneous primary structures along the inner edge of the jet

that contained large amounts of mixed high-speed fluid and homogeneous secondary structures along the outer edge of the jet that contained small amounts of mixed high-speed fluid (Meyer *et al.* 2001). The resulting hybrid p.d.f. shape was stationary (constant peak f_{mHS}) on the high-speed side and marching (varying peak f_{mHS}) on the low-speed side. Unlike the planar mixing layer of the current study, the extent of the stationary p.d.f. region diminished as the axisymmetric mixing layer developed, while the extent of the marching p.d.f. region increased significantly. Since the Kelvin–Helmholtz instability mode diminishes toward the end of the potential core in axisymmetric jets, it is not surprising that the corresponding turbulent-jet p.d.f.s take on a more dominant marching character than in planar shear layers, which have a constant velocity ratio with downstream distance.

Previous probe-based measurements of mixed-fluid statistics in planar shear layers have recorded both stationary-tilted (Konrad 1976; Frieler 1992) and marching (Batt 1977) p.d.f.s. Pickett & Ghandhi (2002) recorded hybrid p.d.f.s at fairly low Re_δ (3300) with tripped or turbulent inlet boundary layers and stationary p.d.f.s with laminar inlet boundary layers. As expected, the large-scale rollers with uniform internal structures were more predominant in the latter case. Observations from the current investigation, as discussed above, indicate that stationary-tilted, marching and hybrid p.d.f.s may exist for various conditions in turbulent shear layers depending on the corresponding large- and intermediate-scale mixing dynamics. Unfortunately, two-dimensional maps of molecular mixing efficiency are not available from previous investigations in gaseous planar shear layers; direct comparisons are possible with respect to ensemble-averaged statistics as discussed further in §6.

5.2. Low-speed vs. high-speed fluid p.d.f.s

It is notable in figure 10 that the character of the high-speed fluid p.d.f.s is different from that of the low-speed fluid p.d.f.s. From the stationary peaks and higher vertical scale of $P(f_{mHS})$, it is clear that the mixed high-speed fluid is spatially more homogeneous and subject to a narrower range of mixed-fluid fractions, respectively, as compared with the mixed low-speed fluid. Significant regions of the mixing layer are at a preferred high-speed mixed-fluid fraction of about 60–65%, with only slight marching behaviour toward the low-speed side. These differences between the low- and high-speed fluid mixing characteristics are consistent with observations regarding the mixed-fluid structure in the instantaneous images of figures 4 to 7. The line plot of figure 8(a), for example, shows low-speed fluid structures with widely varying values of f_{mLS} . The low-speed fluid structures undergo intermittent entrainment so that measurements of mixed-fluid fraction inside the shear layer are likely to yield a wider range of values, with an increasing probability of finding mixed low-speed fluid near the low-speed stream. This low-speed fluid mixing behaviour is in contrast to the more uniform internal structure for the high-speed fluid shown in figure 8(b). Entrainment of high-speed fluid that is more quasi-steady in nature would result in a shear-layer structure that is more uniform in mixed high-speed fluid composition. The inability of passive-scalar measurements to detect differences in low- and high-speed fluid mixing behaviour is discussed further in §5.3, where passive-scalar p.d.f.s of low- and high-speed fluid are presented for comparison with dual-tracer PLIF molecular mixing data.

5.3. Passive-scalar vs. molecularly mixed fluid quantities

Since the NO and acetone PLIF technique can provide molecularly mixed low- or high-speed fluid fractions, it is of interest to compare results from this method with those obtained using the passive-scalar approach with acetone PLIF alone. This can

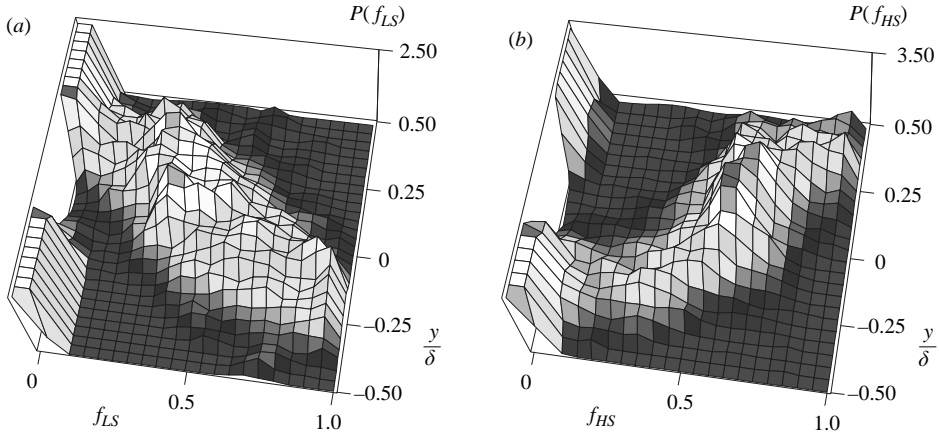


FIGURE 11. Passive-scalar cross-stream p.d.f.s of f_{LS} and f_{HS} for Case 3B ($Re_\delta = 103\,000$, $Rx/\lambda = 28.1$). (a) Low-speed fluid; (b) high-speed fluid.

shed light on the significance of measurement resolution and subresolution stirring when comparing turbulent shear-layer mixing results from previous investigations. For this purpose, p.d.f.s of f_{LS} and f_{HS} from acetone seeding alone are shown in figure 11 for Case 3B ($Re_\delta = 103\,000$, $Rx/\lambda = 28.1$). As noted earlier, passive-scalar methods cannot differentiate between pure and mixed fluid at subresolution scales. For this reason, they are fundamentally unable to define the extent of the molecularly mixed fluid; one must arbitrarily select a passive-scalar value (e.g. 10% to 90%) to do this, depending on the measurement uncertainty of the experiment. To define the extent of the mixing layer in the current work, values of f_{LS} greater than 97% were considered pure (i.e. set to $f_{LS} = 0$), while low values of f_{LS} were allowed to drop to free-stream levels as they were in the dual-tracer PLIF technique. A cutoff margin of 97% was possible because of the relatively high SNRs in the acetone PLIF images on the air side (typically 75:1). This represents an improvement over previous passive-scalar measurements with cutoff margins of 10% and 90% (Clemens & Paul 1995; Karasso & Mungal 1996), and more accurately captures the extent of the mixing layer as the fluid fractions asymptotically approach free-stream levels.

A notable feature in figure 11 is that the p.d.f.s of low- and high-speed fluid are quite similar in character. That is, both f_{mHS} and f_{mLS} display stationary behaviour on the high-speed side and marching behaviour on the low-speed side. In addition, it appears from the passive-scalar p.d.f.s of figure 11 that the fraction of low-speed fluid plus the fraction of high-speed fluid is nearly unity everywhere (as quantified in §6). These trends are in contrast to the data shown in figure 10(b), which display more dissimilar low- and high-speed mixed-fluid p.d.f.s. These observations underscore the importance of measuring molecularly mixed fluid quantities to detect differences in the mixing process between the low- and high-speed fluids, particularly along each interface with the adjacent free-stream fluid.

6. Ensemble-averaged statistics

Further evidence of differences in the mixing behaviour of low- and high-speed fluid can be found by studying ensemble-averaged statistics. To determine the effect of velocity ratio and downstream distance, the statistics of the total mixed-fluid fraction can be obtained by using ensemble-averaged values from the flip experiments.

In addition to analysing the effects of various operating conditions, comparisons are made with data from previous studies. To help in comparisons with previous investigations using acid/base reactions in liquid mixing layers (Koochesfahani & Dimotakis 1986; Karasso & Mungal 1996), low heat release cold-wire measurements in gaseous layers (Mungal & Dimotakis 1984; Frieler 1992), cold-chemistry flip experiments in compressible mixing layers (Clemens & Paul 1995; Island *et al.* 1996), and dual-tracer PLIF experiments in gaseous axisymmetric jets (Meyer *et al.* 2001), a number of definitions are introduced.

By integrating the ensemble average of the mixed-fluid fraction for the images, $\langle f_{mNO} \rangle$, across the mixing layer, it is possible to find the volume fraction of mixed NO-seeded fluid V_{mNO}/V , at various downstream locations:

$$\frac{V_{mNO}}{V} = \frac{\int_{y_1}^{y_2} \langle f_{mNO} \rangle dy}{\delta}, \quad (2)$$

where the subscript 'NO' is replaced with 'LS' or 'HS' if NO is seeded into the low- or high-speed streams, respectively. The ensemble average $\langle f_{mNO} \rangle$ is referred to as the probability of finding mixed NO-seeded fluid, P_{mNO} , at a particular location. The probability of finding mixed fluid of any composition, P_m , is simply the sum of $\langle f_{mNO} \rangle$ from the flip experiments. As shown in equation (3), the ensemble average can also be obtained by integrating the p.d.f.s, $P(f_{mNO})$, over all possible values of f_{mNO} .

$$P_{mLS} = \langle f_{mLS} \rangle = \int_0^1 f_{mLS} P(f_{mLS}) df_{mLS}, \quad (3a)$$

$$P_{mHS} = \langle f_{mHS} \rangle = \int_0^1 f_{mHS} P(f_{mHS}) df_{mHS}, \quad (3b)$$

$$P_m = P_{mLS} + P_{mHS} = \langle f_{mLS} \rangle + \langle f_{mHS} \rangle. \quad (3c)$$

In addition, the average concentration of mixed high-speed fluid, C_m , can be found from equation (4).

$$C_m = \frac{P_{mHS}}{P_m}. \quad (4)$$

Note that $\langle f_{mNO} \rangle$, P_{mNO} , P_m and C_m are functions of x and y . The total volume fraction of mixed fluid, P_M , is defined in equation (5) as the sum of the low- and high-speed fluid mixed volume fractions. The total average high-speed mixed-fluid concentration integrated across the shear layer (often called the mixing efficiency), C_M , is defined in equation (6). The entrainment ratio of high- to low-speed fluid, E , can then be found from equation (7):

$$P_M = \frac{V_{mLS}}{V} + \frac{V_{mHS}}{V}, \quad (5)$$

$$C_M = \frac{V_{mHS}/V}{P_M}, \quad (6)$$

$$E = \frac{C_M}{1 - C_M}, \quad (7)$$

where P_M , C_M and E represent quantities that are integrated across the shear layer, and are functions of x only (streamwise coordinate).

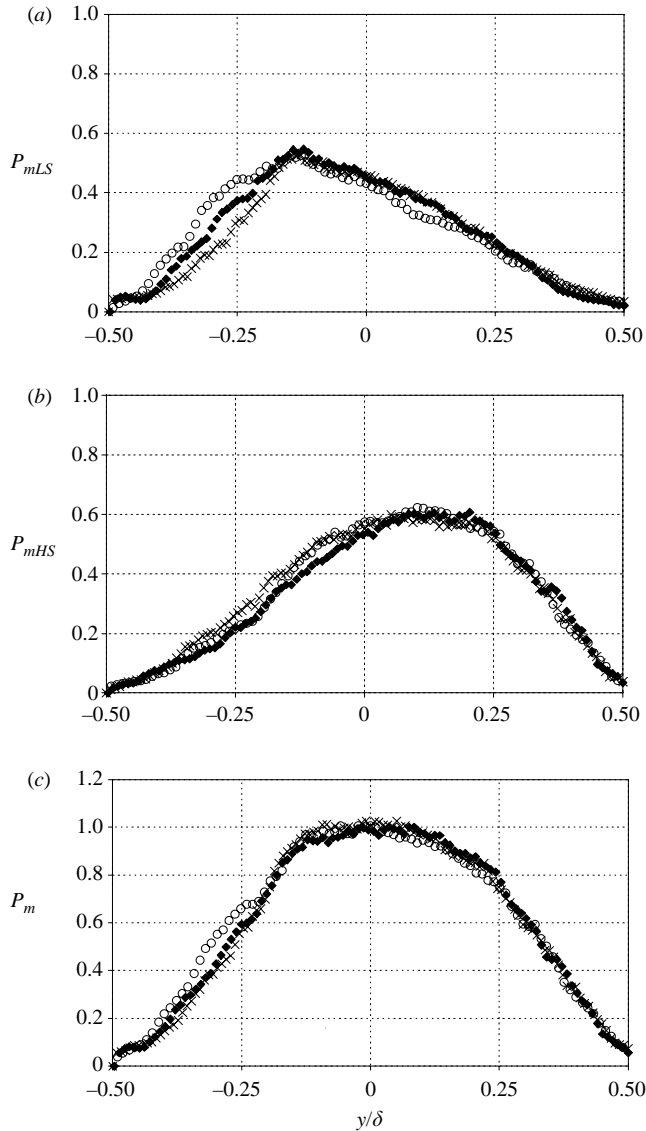


FIGURE 12. Effect of Rx/λ on the (a) low-speed (P_{mLS}) (b) high-speed (P_{mHS}), and (c) total (P_m) mixed-fluid probabilities. \circ , $Rx/\lambda = 14.8$; \blacklozenge , 21.3; \times 28.1.

6.1. Mixed-fluid probability

Mixed-fluid probabilities enable comparisons of the ensemble-averaged spatial distributions of low-speed, high-speed and total molecularly mixed fluid fractions, defined as P_{mLS} , P_{mHS} and P_m , respectively. Figure 12 shows distributions of P_{mLS} , P_{mHS} and P_m for Cases 1B ($Re_\delta = 34\,300$, $Rx/\lambda = 14.8$), 2B ($Re_\delta = 65\,400$, $Rx/\lambda = 21.3$) and 3B ($Re_\delta = 103\,000$, $Rx/\lambda = 28.1$). In terms of differences between the low- and high-speed fluids, P_{mLS} is typically lower than P_{mHS} and is indicative of the preferred entrainment of high-speed fluid into the shear layer. Both P_{mLS} and P_{mHS} peak closer to their respective free streams for all values of Rx/λ , as expected under fully developed conditions. This asymmetry from Rx/λ of 14.8 to 28.1 differs with the results of

Karasso & Mungal (1996) in liquid shear layers, in which they found that the P_{mLS} and P_{mHS} profiles were symmetrical about $y/\delta = 0$ at $Rx/\lambda = 18$, but asymmetric at $Rx/\lambda \geq 30$. The full-width-at-half-maximum (FWHM) of the P_{mHS} curve is also larger than that for P_{mLS} , showing that mixed high-speed fluid is likely to be found over a larger cross-stream extent of the mixing layer, while the molecularly mixed low-speed fluid is confined closer to the low-speed side.

The profiles of total mixed-fluid probability, P_m , as shown in figure 12(c) are nearly unity in the centre of the mixing layer for the three conditions, indicating that unmixed fluid is almost never found in this region. These ensemble-averaged statistics have significantly reduced random error (due to sample size) as compared with instantaneous images, and help corroborate values of η_{mNO} near unity in figures 4 to 7. The finding that very little subresolution stirring of NO-seeded fluid is found in the centre of the mixing layer differs slightly from previous results in gaseous shear layers, which show total mixed-fluid probabilities from cold-chemistry flip experiments to have peak values of 90–95% (Clemens & Paul 1995; Island *et al.* 1996). Those authors did not correct for the finite quenching rate of NO PLIF in the presence of air, however, and state that their measurements underpredict the amount of mixed fluid. Thus, the true peak mixed-fluid probability can be expected to be higher than 90–95% for gaseous flow, as is found in the current study. The results of Karasso & Mungal (1996) in liquid shear layers differ markedly with values of $P_m \approx 50$ –70% in the centre of the mixing layer. In the context of the Broadwell–Bredenthal model, this result implies a decrease in molecular mixing in the interfacial regions between the two fluid streams at high Sc .

With regard to the effect of Re_δ or Rx/λ on the mixed-fluid probabilities, no clear trends are detected in P_{mHS} , with the data in figure 12(b) essentially collapsing for Cases 1B–3B. This is indicative of a self-similar-like character in the high-speed fluid entrainment and mixing processes. The axisymmetric jet results of Meyer *et al.* (2001) showed from axial p.d.f.s that the preferred high-speed fluid mixture fraction was also fully developed by about $Rx/\lambda \approx 12$ –15. In contrast with the high-speed mixed-fluid probabilities, a slight trend is observed in figure 12(a) in which P_{mLS} decreases on the low-speed sides of the profiles from Cases 1B to 3B and increases slightly on the high-speed sides (i.e. the profiles shift to the right). These trends also lead to slight irregularities in the profiles of P_m in figure 12(c). The agreement between Cases 1B to 3B for the mixed fluid probabilities across most of the shear layer, however, is more prominent than the slight trend noted for P_{mLS} .

6.2. Average mixed-fluid composition

The profile of the average mixed-fluid composition, C_m , across the shear layer provides a quantitative measure of the preferential entrainment of low- and high-speed fluids from the corresponding freestreams. The ‘S’-shaped profile in figure 13, with a higher mixed-fluid composition on the high-speed side, is common in both liquid and gaseous shear layers (Mungal & Dimotakis 1984; Karasso & Mungal 1996). Previous measurements in a gaseous shear flow at $Rx/\lambda = 40$ using low heat-release reactions (Mungal & Dimotakis 1984) show a similar mixed-fluid composition of about 0.4 on the low-speed side and 0.7 on the high-speed side. Also in agreement, Island *et al.* (1996) found values ranging from 0.3 to about 0.7 in compressible mixing layers. In contrast, Karasso & Mungal (1996) found much less variation in C_m across a liquid shear layer, with values ranging from 0.5 to 0.6. These variations, which are biased toward the corresponding free-stream fluid, imply that the total mixed-fluid p.d.f.s vary across the shear layer. Since the compositions toward the edges of the

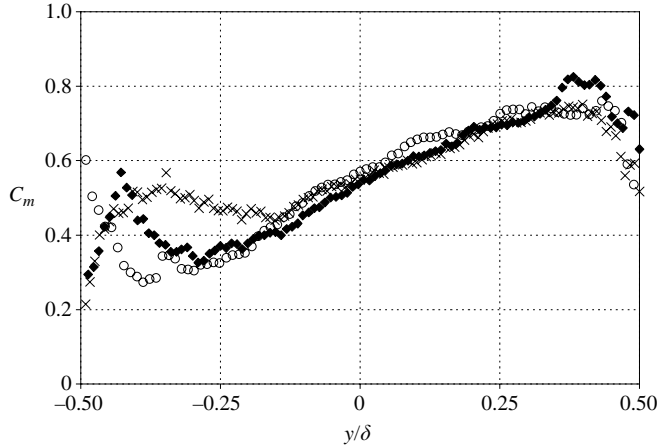


FIGURE 13. Effect of Rx/λ on the averaged high-speed mixed-fluid composition, C_m . Key as in figure 12.

mixing layer do not reach the corresponding free-stream values, Karasso & Mungal (1996) suggest that this implies a ‘tilted’ p.d.f. behaviour rather than a fully marching behaviour. A comparison of C_m profiles between Cases 1B to 3B shows that the shear layer may indeed be slowly evolving. In particular, the shear layer is becoming more homogeneous (less variation in mixed-fluid composition) at higher Re_δ or Rx/λ . This trend is indicative of the increased size and effect of intermediate-scale structures in the molecular mixing process rather than an increase in small-scale turbulent diffusion. The latter would have the opposite effect of increasing the variation of mixed-fluid composition across the shear layer.

Because of the relative lack of subresolution stirring within the mixing layer, it is of interest to determine whether an under-resolved passive-scalar measurement can accurately predict the mixed-fluid composition in gaseous mixing layers. As noted earlier, this issue can be examined in the current work simply by comparing data using acetone PLIF alone with data from simultaneous NO and acetone PLIF. Figure 14 shows that the magnitude of the C_m variation across the shear layer is overpredicted using the passive-scalar method, and is consistent with passive-scalar p.d.f.s exhibiting false marching behaviour, as illustrated in figure 11. In liquid ($Sc \sim 2000$) shear layers, however, Karasso & Mungal (1996) found much more dramatic errors when using the passive-scalar approach. The modest errors shown in figure 14 from the passive-scalar method are not surprising because of the high spatial resolution and high SNRs of the current measurement system, and since the gaseous shear layer is almost entirely molecularly mixed (Clemens & Paul 1995; Island *et al.* 1996). Nonetheless, the mixing rate along the outer region of the shear layer is more closely coupled to chemical reaction rates, and it is this region that displays the greatest potential for error when using the passive-scalar technique.

6.3. Mixed-fluid volume fraction and entrainment ratio

Further comparisons between current data and previous results in gaseous and liquid shear layers can be made regarding the low-speed, high-speed and total mixed-fluid volume fractions, V_{mLS}/V , V_{mHS}/V and P_M , respectively. These were computed using equations (2) and (5), and are shown as functions of Rx/λ in figure 15. Results from cold-wire low heat release studies in gaseous flows ($Sc \sim 1$) show $V_{mLS} \approx 0.25$ and

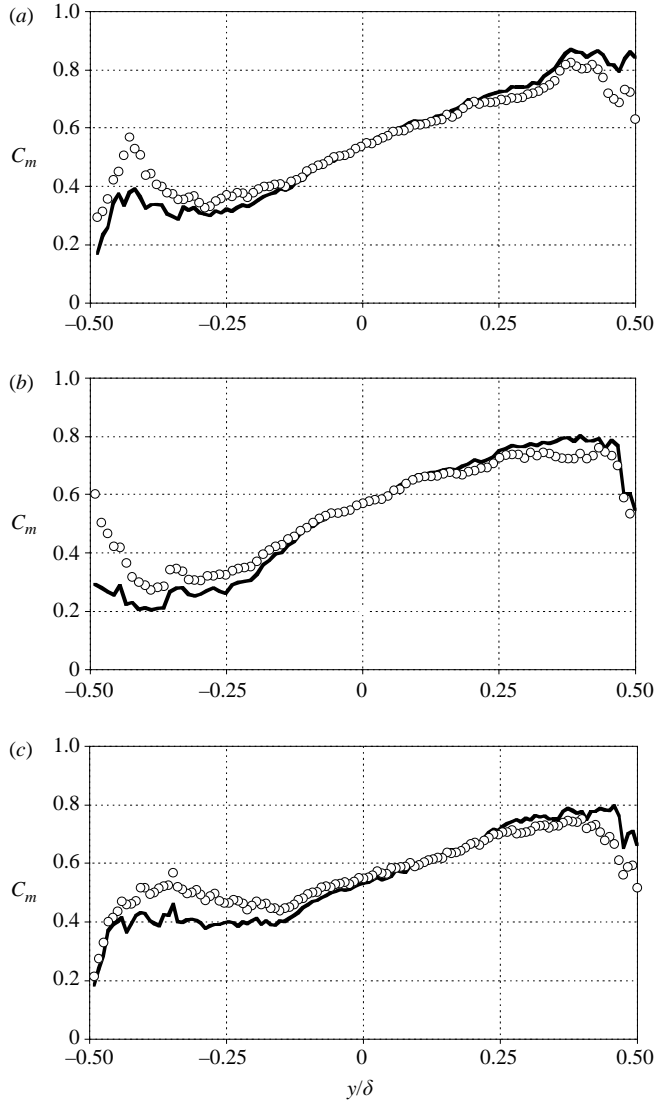


FIGURE 14. Averaged mixed-fluid composition, C_m , from the \circ , dual-tracer and —, passive-scalar methods for (a) Case 1B, (b) Case 2B and (c) Case 3B.

$V_{mHS} \approx 0.30$ in the range of Rx/λ from 16 to 56 (Frierler 1992). These are in good agreement with the results shown in figure 15, which supports the accuracy of the probe-based measurements of Frierler (1992). Similarly for gaseous axisymmetric jets, V_{mHS}/V has been found to vary from 0.25 to 0.28 in the range of Rx/λ from 15 to 30 (Meyer *et al.* 2001). In contrast, V_{mLS}/V and V_{mHS}/V in liquids ($Sc \sim 2000$) are about a factor of two smaller (Karasso & Mungal 1996). The slight drop in V_{mHS}/V , shown in figure 15, is nearly proportional to the drop in P_M as Rx/λ increases. Hence, the total averaged mixed-fluid concentration across the shear layer, C_M , from equation (6), stays nearly constant at 0.55 for Cases 1B to 3B. This corresponds to an entrainment ratio of $E = 1.24$ from equation (7). The model proposed by Dimotakis (1986) predicts values of C_M from 0.55 to 0.58 and values of E from 1.2 to 1.37

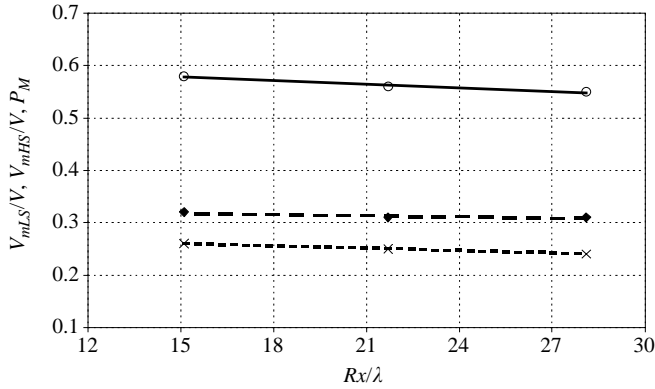


FIGURE 15. Low-speed, high-speed and total mixed fluid volume fractions (\times , V_{mLS}/V ; \blacklozenge , V_{mHS}/V ; \circ , P_M , respectively) as functions of Rx/λ .

for the current flow conditions (see table 1). By comparison, Frieler (1992) obtained values of $C_M \approx 0.5$ to 0.55 ($E \approx 1$ – 1.2) for nearly the same range of velocity ratios as for the current study. Island *et al.* (1996) reported values ranging from $C_M \approx 0.5$ to 0.59 ($E \approx 1$ – 1.44) in compressible mixing layers, while Karasso & Mungal (1996) reported values of $C_M \approx 0.58$ ($E \approx 1.37$) in liquid layers with $r = 0.25$. To first order, these results agree with the ensemble-averaged data from the current investigation. It is likely, therefore, that the molecular-mixing dynamics discussed in §§4 and 5 are applicable to previous studies of shear-layer mixing with similar Reynolds numbers and pairing parameters.

7. Conclusions

The dual-tracer (NO and acetone) PLIF technique employed in the current investigation is the gaseous analogue to acid/base visualizations in liquid flows and is used for the first time to study the role of large- and intermediate-scale structures in determining the state of molecular mixing in the developing and far-field regions of gaseous planar shear layers. Data are compared with acid/base measurements of molecular mixing in liquid planar shear layers, average probe-based measurements in gaseous planar shear layers, and dual-tracer PLIF studies in axisymmetric jets. The current work also reports the first ‘flip’ experiments using the dual-tracer PLIF technique, enabling measurements of gaseous low-speed, high-speed and total fluid molecular mixing. Data are obtained for low- to high-speed velocity ratios from $r = 0.25$ to 0.44 and Reynolds numbers from $Re_\delta = 18\,600$ to $103\,000$, corresponding to pairing parameter values of Rx/λ 6.6 to 28.1. Several key observations are made regarding instantaneous images, probability density functions, and ensemble-averaged statistics of molecularly mixed fluid within the planar shear layer, as enumerated below.

1. There is a very low probability of finding unmixed fluid or subresolution stirring in the centre of the shear layer. Sub-unity values of mixing efficiency, which indicate the presence of subresolution stirring or micro-scale mixing, are found most often in regions adjacent to the low- and high-speed fluid streams. Ensemble-averaged statistics, therefore, show that the total mixed-fluid probability, P_m , is nearly unity in the centre of the mixing layer. This differs most dramatically with previous

measurements in liquid shear layers (Karasso & Mungal 1996), and confirms the effect of Sc at high Re_δ . Slight differences with cold-chemistry flip experiments performed in gaseous shear layers (Clemens & Paul 1995; Island *et al.* 1996) are probably attributable to the inability of previous studies to correct for finite-quenching-rate effects.

2. Owing to the relative absence of subresolution stirring, passive-scalar data are found to compare well with measurements of molecularly-mixed fluid fraction in much of the central region of the mixing layer. The inherent ambiguity in defining the edges of the mixing layer, however, as well as subresolution stirring in the outer regions, still leads to an overprediction of mixed-fluid quantities using the passive-scalar approach.

3. The dynamics of large- and intermediate-scale structures are sensitive to the velocity ratio and have a significant impact on the molecularly mixed fluid distribution within the gaseous shear layer. Intermittent large-scale structures composed of intermediate and small-scale motions are the dominant mechanisms for pure fluid entrainment in both the developing and far-field regions. Intermediate structures generated by secondary instabilities augment fluid entrainment in the outer regions of the mixing layer and, when entrained into the shear layer, are a source of inhomogeneity in mixed-fluid statistics.

4. Both low-speed and high-speed mixed-fluid probability density functions (p.d.f.s) develop stronger marching characteristics with decreased velocity ratio, but are fairly independent of downstream distance, which is consistent with the concept of self-similarity. The transition to marching behaviour is not as prominent as previously found in axisymmetric gaseous shear layers (King *et al.* 1999; Meyer *et al.* 2001).

5. Differences in molecular-mixing behaviour between the low- and high-speed fluids are detected through analyses of p.d.f.s across the shear layer. These differences, as in the range of mixed-fluid fractions exhibited in the low- and high-speed fluid p.d.f.s, are not as apparent in passive-scalar data, which do not account for subresolution-scale molecular mixing.

6. The low- and high-speed mixed-fluid probabilities, P_{mLS} and P_{mHS} , are preferentially higher toward the low- and high-speed streams, respectively. Therefore, the averaged mixed-fluid composition, C_m , is also preferentially higher toward the corresponding free-stream fluid, as found in previous investigations (Mungal & Dimotakis 1984; Karasso & Mungal 1996). The value of P_{mHS} is higher than that of P_{mLS} , confirming that high-speed fluid is preferentially entrained into the shear layer.

7. The effects of Rx/λ on the mixed-fluid probabilities and the mixed-fluid composition are found to be slight from $Rx/\lambda = 14.8$ to 28.1, although a slow reduction in the aforementioned free-stream bias of the low- and high-speed mixed-fluid quantities is detected in C_m . The low-speed, high-speed and total mixed-fluid volume fractions are in agreement with previous measurements in the literature (Frieler 1992; Meyer *et al.* 2001) and remain nearly constant with Rx/λ . These results lend support to a quasi-self-similar state – one that evolves very slowly and is not universally independent of initial conditions.

This work was supported by the National Science Foundation, Division of Chemical and Transport Systems, Grant No. CTS 94-23280, with Dr R. E. A. Arndt and Dr J. F. Foss as Program Monitors. Additional funding was provided by a Ford Foundation Dissertation Fellowship and by Dr J. R. Gord of the Air Force Research Laboratory through a grant from the Air Force Office of Scientific Research (Dr J. M. Tishkoff, Program Manager).

REFERENCES

- BATCHELOR, G. K. 1953 *The Theory of Homogeneous Turbulence*. Cambridge University Press.
- BATT, R. G. 1977 Turbulent mixing of passive and chemically reacting species in a low-speed shear layer. *J. Fluid Mech.* **82**, 53–95.
- BRADSHAW, P. 1966 The effect of initial conditions on the development of a free shear layer. *J. Fluid Mech.* **26**, 225–236.
- BREIDENTHAL, R. 1981 Structure in turbulent mixing layers and wakes using a chemical reaction. *J. Fluid Mech.* **109**, 1–24.
- BROADWELL, J. E. & BREIDENTHAL, R. E. 1982 A simple model of mixing and chemical reaction in a turbulent shear layer. *J. Fluid Mech.* **125**, 397–410.
- BROADWELL, J. E. & MUNGAL, M. G. 1988 Molecular mixing and chemical reactions in turbulent shear layers. *Twenty-Second Symposium (International) on Combustion*, pp. 579–587. The Combustion Institute.
- BUCH, K. A. & DAHM, W. J. A. 1996 Experimental study of the fine-scale structure of conserved scalar mixing in turbulent shear flows. Part 1. $Sc \gg 1$. *J. Fluid Mech.* **317**, 21–71.
- BUCH, K. A. & DAHM, W. J. A. 1998 Experimental study of the fine-scale structure of conserved scalar mixing in turbulent shear flows. Part 2. $Sc \sim 1$. *J. Fluid Mech.* **364**, 1–29.
- CLEMENS, N. T. & MUNGAL, M. G. 1995 Large-scale structure and entrainment in the supersonic mixing layer. *J. Fluid Mech.* **284**, 171–216.
- CLEMENS, N. T. & PAUL, P. H. 1995 Scalar measurements in compressible axisymmetric mixing layers. *Phys. Fluids* **7**, 1071–1081.
- DAHM, W. J. A., SOUTHERLAND, K. B. & BUCH, K. A. 1991 Direct, high resolution, four-dimensional measurements of the fine scale structure of $Sc \gg 1$ molecular mixing in turbulent flows. *Phys. Fluids A* **3**, 1115–1127.
- DIMOTAKIS, P. E. 1986 Two-dimensional shear-layer entrainment. *AIAA J.* **24**, 1791–1796.
- DIMOTAKIS, P. E. 2000 The mixing transition in turbulent flows. *J. Fluid Mech.* **409**, 69–98.
- DZIOMBA, B. & FIEDLER, H. E. 1985 Effect of initial conditions on two-dimensional free shear layers. *J. Fluid Mech.* **152**, 419–442.
- FRIELER, C. E. 1992 Mixing and reaction in the subsonic 2-d turbulent free shear layer. PhD thesis, California Institute of Technology, Pasadena, California.
- GUTMARK, E. & HO, C. M. 1983 Preferred modes and the spreading rates of jets. *Phys. Fluids* **26**, 2932–2938.
- HU, H. & KOCHESFAHANI, M. M. 2002 A novel method for instantaneous, quantitative measurement of molecular mixing in gaseous flows. *Exps. Fluids* **33**, 202–209.
- HUANG, L. S. & HO, C. M. 1990 Small-scale transition in a plane mixing layer. *J. Fluid Mech.* **210**, 475–500.
- HUSSAIN, A. K. M. F. & ZAMAN, K. B. M. Q. 1980 Vortex pairing in a circular jet under controlled excitation. Part 2. Coherent structure dynamics. *J. Fluid Mech.* **101**, 493–544.
- ISLAND, T. C., URBAN, W. D. & MUNGAL, M. G. 1996 Quantitative scalar measurements in compressible mixing layers. *AIAA Paper* 96-0685.
- KARASSO, P. S. & MUNGAL, M. G. 1996 Scalar mixing and reaction in plane liquid shear layers. *J. Fluid Mech.* **323**, 23–63.
- KING, G. F., DUTTON, J. C. & LUCHT, R. P. 1999 Instantaneous, quantitative measurements of molecular mixing in the axisymmetric jet near field. *Phys. Fluids* **11**, 403–416.
- KING, G. F., LUCHT, R. P. & DUTTON, J. C. 1997 Quantitative dual-tracer planar laser-induced fluorescence measurements of molecular mixing. *Opt. Lett.* **22**, 633–635.
- KOLMOGOROV, A. N. 1941 On degeneration (decay) of isotropic turbulence in an incompressible viscous liquid. *Dokl. Akad. Nauk SSSR* **31**, 538–540.
- KONRAD, J. H. 1976 An experimental investigation of mixing in two-dimensional turbulent shear flows with applications to diffusion-limited chemical reactions. PhD thesis, California Institute of Technology, Pasadena, California.
- KOCHESFAHANI, M. M. & DIMOTAKIS, P. E. 1986 Mixing and chemical reactions in a turbulent liquid mixing layer. *J. Fluid Mech.* **170**, 83–112.
- LOZANO, A., YIP, B. & HANSON, R. K. 1992 Acetone: a tracer for concentration measurements in gaseous flows by planar laser-induced fluorescence. *Exps. Fluids* **13**, 369–376.

- MASUTANI, S. M. & BOWMAN, C. T. 1986 The structure of a chemically reacting plane mixing layer. *J. Fluid Mech.* **172**, 93–126.
- MEHTA, R. D. 1991 Effect of velocity ratio on plane mixing layer development: influence of the splitter plate wake. *Exps. Fluids* **10**, 194–204.
- MEHTA, R. D., INOUE, O., KING, L. S. & BELL, J. H. 1987 Comparison of experimental and computational techniques for plane mixing layers. *Phys. Fluids* **30**, 2054–2062.
- MEYER, T. R. 2001 Turbulent molecular mixing in gaseous free shear flows. PhD thesis, University of Illinois at Urbana-Champaign, Urbana, Illinois.
- MEYER, T. R., DUTTON, J. C. & LUCHT, R. P. 1999 Vortex interaction and mixing in a driven gaseous axisymmetric jet. *Phys. Fluids* **11**, 3401–3415.
- MEYER, T. R., DUTTON, J. C. & LUCHT, R. P. 2001 Experimental study of the mixing transition in a gaseous axisymmetric jet. *Phys. Fluids* **13**, 3411–3424.
- MEYER, T. R., KING, G. F., MARTIN, G. C., LUCHT, R. P., SCHAUER, F. R. & DUTTON, J. C. 2002 Accuracy and resolution issues in NO/Acetone PLIF measurements of gas-phase molecular mixing. *Exps. Fluids* **32**, 603–611.
- MOSER, R. D. & ROGERS, M. M. 1991 Mixing transition and the cascade to small scales in a plane mixing layer. *Phys. Fluids A* **3**, 1128–1134.
- MUNGAL, M. G. & DIMOTAKIS, P. E. 1984 Mixing and combustion with low heat release in a turbulent shear layer. *J. Fluid Mech.* **148**, 349–382.
- OLSEN, M. G. 1999 Planar velocity measurements in an incompressible and weakly compressible mixing layer. PhD thesis, University of Illinois at Urbana-Champaign, Urbana, Illinois.
- PAUL, P. H. & CLEMENS, N. T. 1993 Sub-resolution flowfield measurements of unmixedness using electronic quenching of NO $a^2\sigma^+$. *Opt. Lett.* **18**, 161–163.
- PICKETT, L. M. & GHANDHI, J. B. 2002 Passive scalar mixing in a planar shear layer with laminar and turbulent inlet conditions. *Phys. Fluids* **14**, 985–998.
- ROGERS, M. M. & MOSER, R. D. 1994 Direct simulation of a self-similar turbulent mixing layer. *Phys. Fluids* **6**, 903–923.
- SEITZMAN, J. M., MILLER, M. F., McMILLIN, B. K., HANSON, R. K., DEBARBER, P. A. & HESS, C. F. 1994 Multiple scalar planar fluorescence imaging for reacting flows. *AIAA Paper* 94-0228.
- SLESSOR, M. D., BOND, C. L. & DIMOTAKIS, P. E. 1998 Turbulent shear-layer mixing at high Reynolds numbers: effects of inflow conditions. *J. Fluid Mech.* **376**, 115–138.
- WIECEK, K. C. & MEHTA, R. D. 1998 Effects of velocity ratio on mixing layer three-dimensionality. *Expl. Therm. Fluid Sci.* **16**, 165–176.
- YIP, B., LOZANO, A. & HANSON, R. K. 1994 Sensitized phosphorescence: a gas phase molecular mixing diagnostic. *Exps. Fluids* **17**, 16–23.